Materials Today • Volume xxx, Number xx • xxxx 2025

ELSEVIER

Supersonic puncture-healable and impact resistant covalent adaptive networks

Zhen Sang [a,c], Hongkyu Eoh [a], Kailu Xiao [a], Dmitry Kurouski [b], Wenpeng Shan [a], Jinho Hyon [a], Svetlana A. Sukhishvili [a,*], Edwin L. Thomas [a,*]

[a] Department of Materials Science & Engineering, Texas A&M University, College Station, Texas 77843, United States
[b] Department of Biochemistry and Biophysics, Texas A&M University, College Station, Texas 77843, United States
[c] Department of Chemistry, Massachusetts Institute of Technology, Cambridge, MA 02139, United States

The dynamic behavior of thin polymer films under high-rate deformation and at small length scales is quite different from that of macroscopic samples loaded quasi-statically. While self-healing of dynamic polymers is well documented for macroscopic samples under applied pressure, mild temperature, and prolonged times, self-healing at the nanoscale after extreme deformation at high rates is largely unexplored. We demonstrate the extensive puncture healing of furan/maleimide Diels-Alder polymer (DAP) covalent adaptive network (CAN) submicron thin films induced by supersonic micro-projectile impacts. For a given sample thickness to projectile size ratio, DAP submicron thin films display a significantly smaller perforation than glassy thermoplastics while showing adequate kinetic energy absorption. Post-mortem microscopic examination reveals efficient puncture healing that is enabled by spatiotemporal gradients in stress- and temperature-induced thermomechanical responses of DAP networks. These responses include a unique solid-to-liquid transition, in addition to viscoelasticity and viscoplasticity. Dissociation of DA bonds occurs due to adiabatic heating and high stresses. The partially dissociated network undergoes biaxial stretching until perforation with subsequent entropically-driven elastic recovery helping puncture closure. Infrared nanospectroscopy confirms that the chemical structure of DAP networks surrounding the puncture has recovered to that before the impact. The energy absorption is evaluated using in-situ imaging at nanosecond, micron-scale resolution. This work suggests molecular design principles for advanced self-healable, damage-tolerant, and energy-absorptive materials that withstand ballistic impacts.

Keyword: hypervelocity; dynamic covalent networks; puncture healing

Introduction

The resilience of materials to high-velocity impact is critical in applications from military to space protection. Crewed spacecraft in low earth orbit, for example, often experience impacts by micrometeoroids (10 μm – 1 mm) that travel at an average speed of 10 km/s that result in high strain rate (HSR) deformation (strain rate, $\dot{\varepsilon} = 10^4 - 10^7\ s^{-1}$). [1,2] If the kinetic energy (KE) of the debris is only partially dissipated by the protective materials, a large diameter perforation can lead to rapid pressure loss. Therefore, designing materials that are not only impact-resilient but also ultrafast self-healable is critical for the crew safety. Our strategy is to explore the ballistic impact behavior of polymeric materials that exhibit strain-rate-dependent deformation behavior [3] with the ability to self-heal [4]. The self-healing behavior of polymers largely relies on the network design in which different types of secondary bonds are often incorpo-

* Corresponding authors.
E-mail addresses: Sukhishvili, S.A. (svetlana@tamu.edu), Thomas, E.L. (elt@tamu.edu).

 https://doi.org/10.1016/j.mattod.2024.12.006

Please cite this article in press as: Z. Sang et al., Materials Today (2025), https://doi.org/10.1016/j.mattod.2024.12.006

rated, including hydrogen bonding, ionic coordination, π-π interactions, and van der Waals interactions. [5–8] Dynamic responses of these bonds to HSR deformation have been explored in several polymeric systems at the macroscopic scale. For instance, elastomeric poly(ethylene-co-methacrylic acid) (EMAA) ionomers, a commercial product Surlyn, originally developed by DuPont, exhibit hydrogen bonding and ionic interactions. These secondary bonds support up to 100 % closure of perforation of mm thick samples under $\dot{\varepsilon} \sim 10^4$ s^{-1} due to fast ($t < 100$ μs) entropy-driven elastic recovery followed by melt flow interdiffusion [9,10]. However, EMAA lacks adequate KE absorption, with a mass-normalized KE absorption of less than 0.3 MJ kg^{-1} under impact velocities of 962 m/s in gas gun experiments on 4.9 mm thick plates [11]. An extreme example of a material with high hydrogen bonding density, crystalline polyparaphenylene terephthalamide (e.g., Kevlar), with Young's modulus in the range ~ 10 GPa, can demonstrate a somewhat higher KE absorption exceeding 0.5 MJ kg^{-1} [12], but lacks self-healing due to limited mobility of the rigid-rod crystalline polymer chains and absence of entropic chain memory.

Wudl et al. [13] pioneered using furan and maleimide functionalized units to create crosslinked networks of Diels-Alder (DA) reversible covalent bonds and demonstrated multiple "remending" cycles of mechanically propagated cracks. Since this early work, numerous types of dynamic covalent bonds have been introduced to create self-healable polymer networks, com-

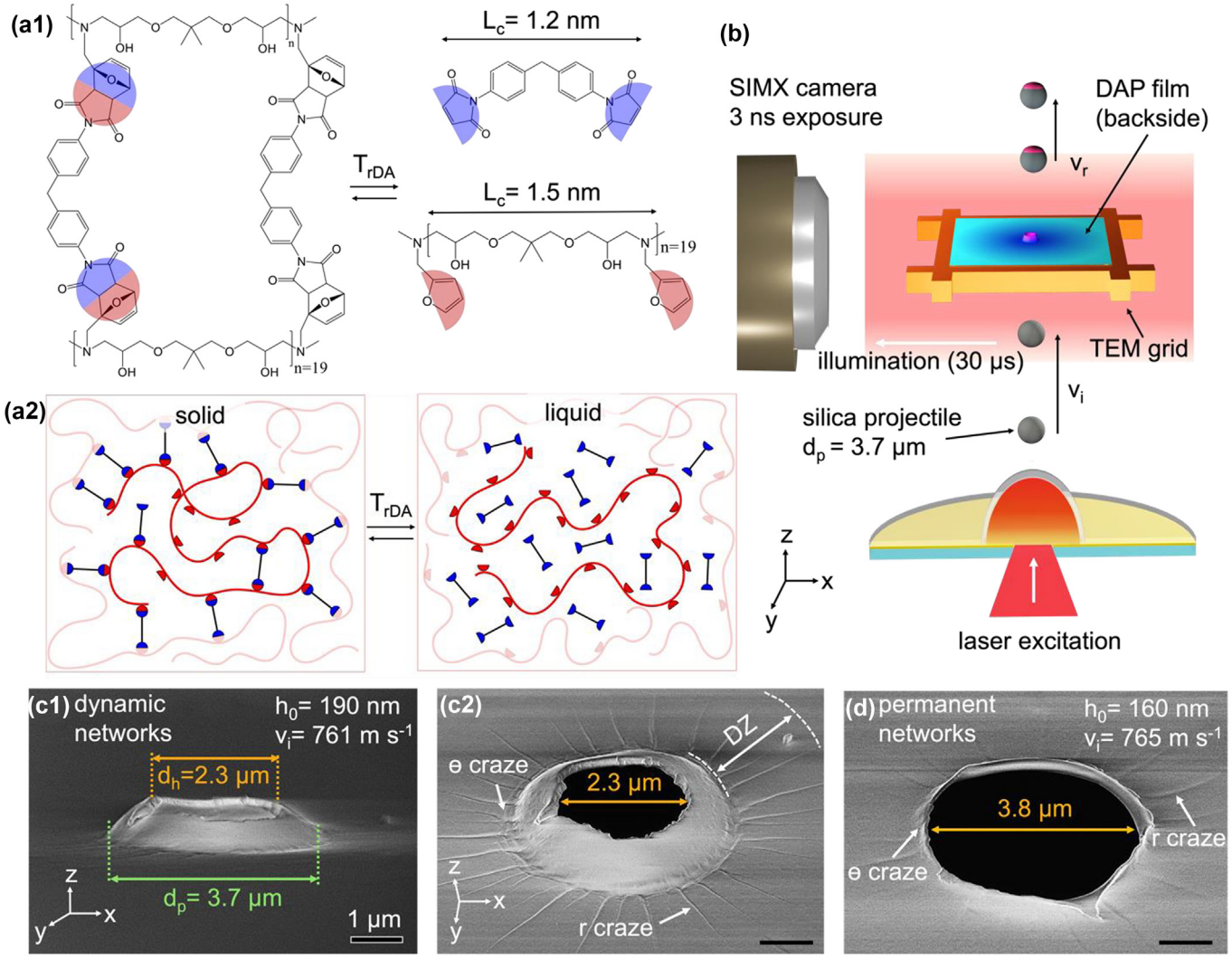

FIG. 1

DAP networks, LIPIT apparatus, and perforation morphology of impacted DAP thin film. a Chemical structure of DAP networks (maleimide to furan ratio (χ_{BMI}) = 0.7) which completely dissociate to viscous liquid at T_{rDA} = 116 °C consists of furan-attached prepolymers (~7000 g mol^{-1} , repeat unit contour length (L_c = 1.5 nm)) and BMI crosslinkers (L_c = 1.2 nm). **b** Schematic of the LIPIT apparatus showing Au-ablation-induced instantaneous volume expansion of the elastomer launching pad for a 3.7 μm silica projectile directed towards a DAP 0.7 film, and the progression of the projectile during impact as recorded by an ultra-high frame rate camera. **c-d** SEM images of the film backsides taken at tilts of 85° (c1) and 52° (c2) for a DAP 0.7 film (h_0 = 190 nm) and permanent crosslinked DDM 0.7 film (h_0 = 155 nm) (d, 52°) impacted at ~ 760 m/s . Both radial (r) and circumferential (θ) crazes are evident. The DAP 0.7 film showed a perforation (orange arrow, d_h = 2.3 μm) smaller than the projectile diameter (d_p = 3.7 μm, green arrow); by contrast, a perforation matched to d_p was observed for DDM film.

Please cite this article in press as: Z. Sang et al., Materials Today (2025), https://doi.org/10.1016/j.mattod.2024.12.006

monly referred to as covalent adaptive networks (CANs) or as dynamic covalent polymer networks. [14,15] Dynamic covalent bonds that re-shuffle by the dissociative mechanism (such as DA bonds) are stable at ambient conditions but become dynamic under increased temperature and stress [14,16–18]. Bond dissociation vs bond reformation depends on both the temperature and stress level. The "self-healing" of macroscopic samples fractured at quasi-static rates ($\dot{\varepsilon} < 10^0$ s^{-1}) is typically conducted under "non-self" alignment of the fractured surfaces, application of a contact pressure, and often includes heating the sample for a prolonged time [4,13,19]. To date, the dynamic responses of CANs under high strain rate (HSR) deformation remain largely

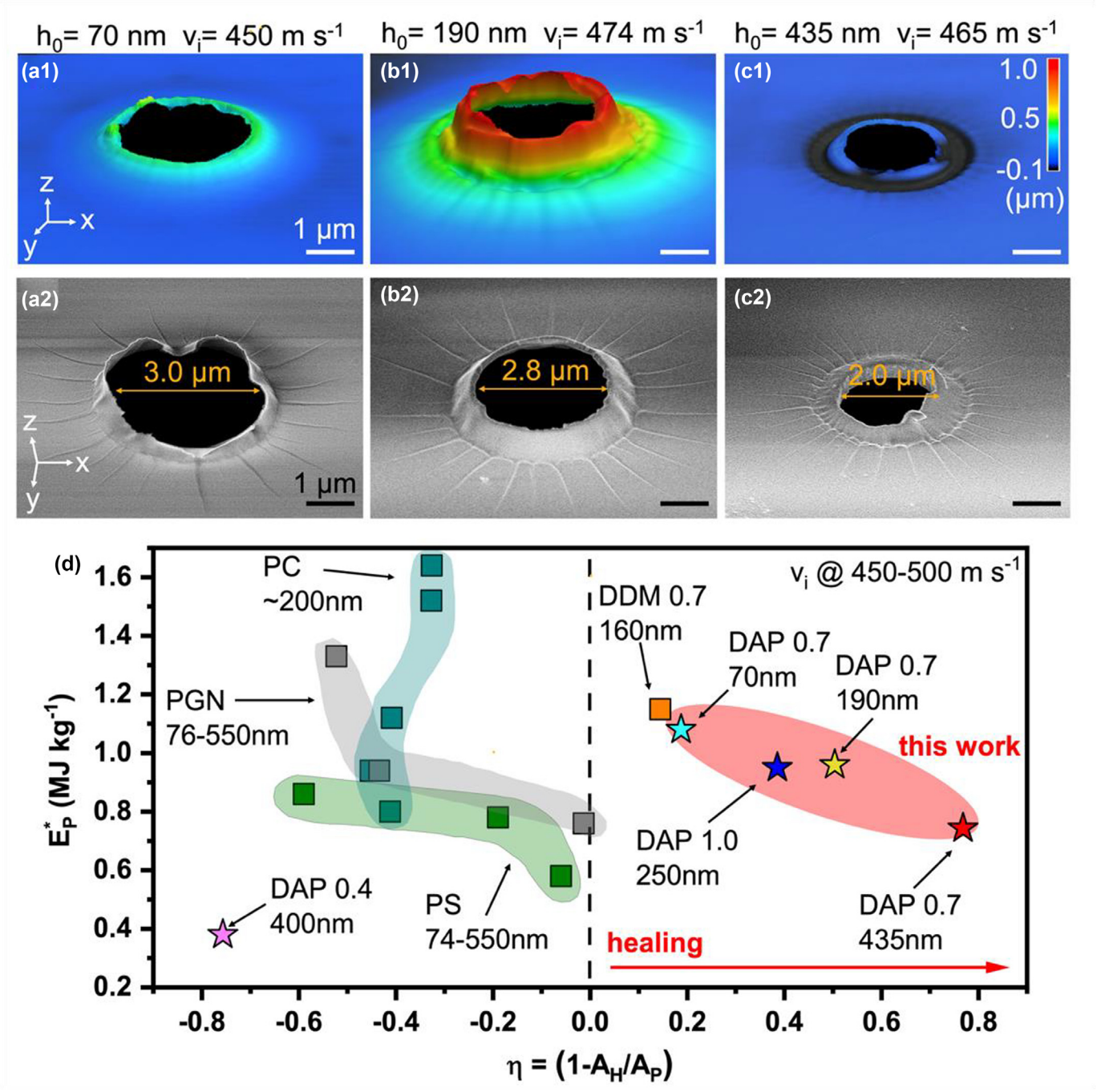

FIG. 2

Post-mortem morphology and comparison of puncture-healing efficiency and KE absorption ability. a-c 66° tilted confocal and 52° tilted SEM images for two sets of films with h_0 = 70, 190, and 435 nm films impacted at ~ 460 m/s . All samples showed smaller diameter perforations (d_h) than the diameter of the projectile (d_p). d Puncture-healing efficiency η (1- A_h /A_p) plotted against specific energy absorption E_p * (MJ kg^{-1}) impact velocity v_i at 450–500 m/s for DAP films versus literature LIPIT experiments (refs. [20,21,29,31] details in Supplementary Table 1 and Fig. S9). DAP 0.7 showed substantial healing/closure with a healing efficiency reaching 0.8 and had similar E_p * values compared to PS, PC, and PGN thermoplastic films. The projectile size is 3.7 μm for all samples, except for PC, which utilized a 7.6 μm silica projectile.

Please cite this article in press as: Z. Sang et al., Materials Today (2025), https://doi.org/10.1016/j.mattod.2024.12.006

unexplored. Laser-induced microprojectile impact testing (LIPIT) where a hard spherical projectile impacts a thin, deformable target film, subjects the sample to ultra-high strain rates ($\dot{\varepsilon} > 10^7\ s^{-1}$) which causes extreme transient temperature, pressure and deformation gradients during the impact event [20]. In LIPIT experiments on DA polymers (DAPs), the adiabatic shock and viscoplastic work will rapidly elevate sample temperature and stress, thus creating significant gradients in crosslink density due to bond dissociation. Subsequent sample deformation, energy dissipation and recovery will depend on the interplay of network breakdown vs. entropic recovery along with DA bond reassociation and network reformation. Due to the small size of the impact region and the short event time in LIPIT, strong gradients over length and time scales present unique thermomechanical environments that together influence puncture healing and energy dissipation in the film.

Moreover, HSR deformation and energy dissipation behaviors of materials are found to be thickness dependent. For instance, macroscopic glassy polystyrene (PS) is brittle at room temperature (RT), while, surprisingly, sub-100-nm well-entangled PS thin film absorbs a KE/mass up to 2.8 MJ kg^{-1} in LIPIT experiments [21]. In PS thin films, in addition to energy-dissipative shear banding and crazing, the reduced entanglements and higher mobility of polymers in the near-surface region facilitate the formation of viscoelastic melt under adiabatic shock and viscoplastic-work-induced heating, resulting in enhanced ductile failure and higher KE absorption per unit mass compared to macroscopic samples. Thus, it is of significant interest to fabricate and explore the puncture-healing and energy dissipation behavior of DAP ultrathin films subjected to supersonic μ-projectile impact.

We report the dynamic response of nanometer-scale thickness DAP films and their ultrashort time puncture healing performance under μ-projectile impacts at 300–750 m/s ($\dot{\varepsilon} > 10^7\ s^{-1}$). Silica projectiles with a diameter of 3.7-μm are launched toward a thin film (75–435 nm) target and the impact is observed in real-time using a micrometer- and nanosecond-resolution ultrahigh frame rate (UHFR) camera. We then employ post-mortem characterization techniques, including laser confocal scanning microscopy (LCSM) and scanning electron microscopy (SEM), as well as infrared nanospectroscopy (AFM-IR), to examine film morphology, to quantify the self-healing behavior, and detect dynamic bond recovery. The real-time impact observations and post-mortem analysis of the puncture regions enabled us to propose DAP-enabled mechanisms and generalize future design principles for puncture-healable and energy-dissipative resilient materials under supersonic impact.

Ultra-thin Diels-Alder polymer films and their post-impact morphology

While the field of dynamic polymer networks has been vigorously developing in the past decade, it has been largely limited to studies of macroscopic bulk material. [22–24] Thus, the chemical fabrication of nanoscale ultrathin films of dynamic polymer networks is the first challenge. We take advantage of the dissociative nature and temperature sensitivity of the catalyst-free DAP networks to adapt them to conventional thin-film fabrication methods, such as spin-coating. Unlike certain associative CANs (e.g., vitrimers) where catalysts are often required [22,24] and the networks are solvent-resistant [23], DAP networks (Fig. 1a) can be fully dissolved in a mixture of toluene and dimethylformamide (DMF) by heating to the T_{rDA} = 116 °C. During dissolution, networks reversibly deconstruct into low-molecular-weight prepolymers bearing furan moieties (MW ~ 7,000 g mol^{-1}) and bismaleimide (BMI, MW = 358 g mol^{-1}) crosslinkers, which during subsequent solvent evaporation and annealing, reversibly re-construct. By simply adjusting the DAP concentration, ultra-thin films with a wide range (70–435 nm) of controllable thickness were obtained (Fig. S1). The quasi-static mechanical properties of the films were explored by the wrinkling method [25,26] (Fig. S2 a-c). Network formation was confirmed by attenuated total reflectance (ATR)-FTIR spectroscopy (Fig. S2d) with identical characteristic peaks as macroscopic DAP materials [27,28].

The HSR dynamic behavior of DAP thin films was studied using LIPIT at ambient conditions (Fig. 1b) [20,21,29,30]. We adjusted the crosslinker density by changing the molar ratio of maleimide to furan (χ_{BMI}) from 0.4 to 0.7 to 1.0, resulting in T_g varying from 8 to 35, and 40 °C while all networks have the same T_{rDA} at 116 °C. The initial sample explored was a glassy DAP 0.7 network. Interestingly, when a DAP 0.7 film with a thickness (h_0) of 190 nm was impacted at a velocity (v_i) of 761 m/s, the post-mortem backside view of tilted SEM images (Fig. 1c) illustrated a puncture-healing behavior of the film, with a perforation hole diameter (d_h) of 2.3 μm, 38 % smaller than the projectile diameter (d_p). Backside imaging of the impact region revealed an upward-oriented conical frustum deformation morphology, with a smooth outer surface and relatively uniformly fractured edge around the periphery of the perforation (Fig. 1c1), while the area outside the impact region contained many localized deformation zones (DZs, radial (r) crazes) and circumferential (ɵ) crazes) (Fig. 1c2). The partially puncture-healed morphology with a perforation diameter smaller than the projectile diameter is unique and not observed with other glassy polymers tested by LIPIT, including polystyrene (PS) [21], PS-grafted nanoparticles (PNG) [20], polymethyl methacrylate (PMMA) [29], and polycarbonate (PC) [31], where typically the backside images reveal adiabatic-heating-induced viscoelastic-viscoplastic melt (flaps) and fibrils, oriented along the radial direction, folded over and fused to the adjacent film, with typical perforations up to 50 % larger than projectile diameters.

To contrast the role of covalent dynamic bonds in forming such partially healed puncture closures, a permanent covalently crosslinked film was prepared using 4,4′- diaminodiphenylmethane (DDM) at the same molar ratio as BMI in DAP 0.7 (Fig. 1d and S3), with a thickness and glass transition temperature (h_0 = 160 nm, T_g = 33 °C) nearly matching those of DAP 0.7 (h_0 = 190 nm, T_g = 35 °C). DDM 0.7 films showed poor puncture-healing behavior at similar impact velocities. For example, DDM 0.7 exhibited a perforation ~ 50 % larger than that of DAP 0.7 at 761 m/s. DDM 0.7 films had a nearly flat perforation with shallow radial and circumferential crazes reflecting the limited mobility and inability to thermally dissociate/associate the permanently crosslinked network.

Please cite this article in press as: Z. Sang et al., Materials Today (2025), https://doi.org/10.1016/j.mattod.2024.12.006

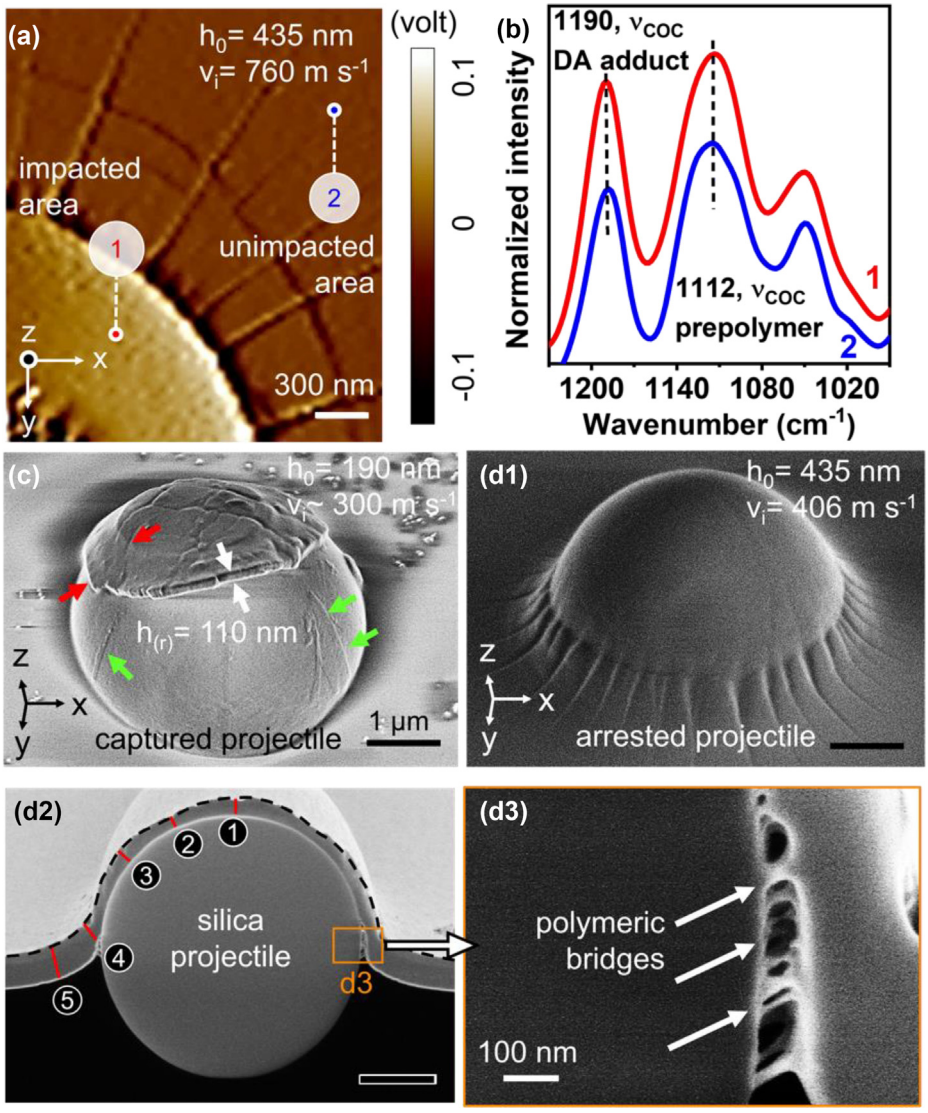

FIG. 3

Understanding puncture healing behavior via chemical and morphological analysis. a Representative AFM-IR deflection map of a 435-nm film impacted at 760 m/s . The red and blue dots indicate the measurement positions and are located closer and further from the perforation, respectively. **b** The similarity of the spectra suggests retention of the dynamic bond chemical identity after perforation. **c** Top-view SEM image of a captured projectile stuck to the carbon tape capture plate after perforating a 190-nm film at v_i ~ 300 m/s . The adhering film cap shows crazes near the center surrounded by a smoothed region due to plastic flow (h_r = 110 nm, corresponding to a local biaxial strain of ~ 130 %). Green arrows indicate longitudinally oriented and flattened fibril-ribbons adhering to the projectile surface. **d** SEM and FIB-SEM images for a 435-nm film impacted at 406 m/s . (**d1**) Arrested projectile with conformed DAP film. The adiabatic heating and biaxial stretching caused the erasure of crazes and shear bands in the cap region. (**d2**) A tilt-corrected FIB diametrical cross-section image of the sample in **d1**. The upper film surface appears bright due to the metal protection coating applied for FIB milling. Position 2 had the smallest h_r / h_0 of 0.3 among positions 1–5, representing a biaxial stretching of about 170 %. (**d3**) Polymer bridges of variable lengths and diameters connect from the film frontside to the projectile.

Puncture-healing and energy absorption performance

Fig. 2 summarizes the results of post-mortem morphological analysis, puncture-healing efficiency, and kinetic energy absorption ability of various types of DAP films with different thicknesses and molar ratios. The perforated films were studied using a non-destructive LCSM prior to SEM to avoid the effect of electron-beam-induced damage [32]. LCSM images (Fig. 2a1-c1) with corresponding height profiles (h_z) (Fig. S4) illustrate the surface morphology of a series of DAP 0.7 films (h_0 = 70–435 nm) impacted at ~ 460 m/s. Thinner films (≤ 190 nm, Fig. 2b2) tended to form the conical frustum morphology due to their plastic compliance with the forward motion of the projectile, whereas a thicker 435-nm film remained relatively planar. SEM images indicate that thinner 70-nm and thicker 435-nm DAP 0.7 films (Fig. 2a2 and c2) were able to exhibit partial puncture-healing behavior, with 20 and 50 % reductions of perforation hole diameter as compared to the projectile diameter. Puncture-healed surface deformation morphologies for a series of film thicknesses and impact velocities are shown in Fig. S5. Note that the observed post-mortem morphologies of DAP films

Please cite this article in press as: Z. Sang et al., Materials Today (2025), https://doi.org/10.1016/j.mattod.2024.12.006

are consequences of nanosecond-scale increases in temperature and stress under HSR deformation and subsequent partially dissociated network entropic relaxation and bond reformation during cooling. Figs. S6 and S7 show that DAP networks demonstrated strong sensitivity to temperature and shear, respectively. Further time-dependent morphological changes of punctures were observed with post-annealing for hours at 70 °C, where DA bond re-shuffling was activated (Fig. S8).

To quantify the supersonic puncture healing performance, the puncture-healing efficiency is defined as $\eta = (1- A_h/A_p)$, where A_h is the top-view perforation area, and A_p is the projectile diametrical cross-sectional area. Fig. 2d shows that DAP 0.7 films impacted at ~ 450 m/s demonstrated puncture-healing behavior, especially the 435-nm (red star) that exhibited η values up to 0.8, outperforming its permanently crosslinked counterpart (DDM 0.7), as well as previously reported glassy polymer thin films [20,21,31]. Across the entire velocity range, the efficiency of healing increased with h_0/d_p ratio and was almost independent of v_i, as shown in Figs. S9a and S10 and Supplementary Table 1. By contrast, a strong v_i dependence of puncture healing was observed for thicker PS and PGN films, where partial healing occurred only with 550-nm thick film impacted at 830 m/s, likely due to v_i- and h_0-related stress localization. Additional parameters for evaluating puncture healing include mass preservation and extent of bond recovery. The mass retention of the target material was studied by using a focused ion beam (FIB) to reveal the variation of the film thickness across the impact region. Fig. S11 shows a centerline cross-section image for perforated 435-nm-thick films. Based on the thickness profile, about 65 and 80 % of the mass of the film was preserved for impact velocities of 504 and 765 m/s, respectively, based on the projected film volume ($V = h_0\pi d_p^2/4$) beneath the projectile.

We utilized resonance-enhanced AFM-IR [33] – a technique with high spatial resolution (sub-20 nm) and sensitivity, thus uniquely suited for studying μ-projectile impacted thin films to probe the retention of DAP chemical characteristics in the local film area that experienced elevated temperatures due to adiabatic shock and viscoplastic work. AFM-IR spectra were taken from the two locations in the film impacted at 760 m/s, shown in Fig. 3a, one within (1, red) and one away from (2, blue) the impact area. As seen in Fig. 3b, the AFM-IR spectra within a detected volume (1×10^5 nm^3) beneath the AFM tip showed the same characteristic peaks as observed by ATR-FTIR for bulk DAP (Fig. S2d), and the IR profiles at the red and blue locations were identical, suggesting no permanent chemical changes in DAP films after the impact. This result might seem to contradict the thermogravimetric analysis (TGA) data in Fig. S12, showing that decomposition/weight loss of DAP networks occurs above 250 °C. However, as predicted by finite element simulations, in LIPIT experiments, thin film materials experience extreme temperatures for only a few nanoseconds [34], i.e., thus at a time scale 10–11 orders of magnitude shorter than during the TGA measurements (heating rate of 10 °C min^{-1}), therefore the material experiences very limited chemical degradation. The AFM-IR measured the bond reformation in the elastically recovered area. This does not eliminate the possibility of degradation in the material carried away on the projectile. The ability of DAP materials to demonstrate substantial puncture area closure, mass preservation, and bond recovery emphasizes their potential to tolerate multiple impacts.

The UHFR camera was used to determine the velocities of the projectile before and after perforation (v_i and v_r, respectively) for calculating the specific kinetic energy absorption (E_p^* in MJ kg^{-1}) (Supplementary Table 1 and Fig. S13). In Fig. S9b, the overall E_p^* performance of DAP 0.7 films for all v_i and h_0 was at a similar level as the earlier reported glassy thermoplastic polymer thin films [20,21,31]. The E_p^* values of DAP increased with higher v_i but decreased with thicker h_0. For example, Fig. 2d shows a 70-nm DAP 0.7 film impacted at 450 m/s had an E_p^* value of 1.1 MJ kg^{-1}, 48 % higher than the 435-nm film at the same v_i. The relatively uniform heating and large temperature rise in thin films aid bond dissociation and increase the amount of viscoplastic network per unit volume, enhancing energy dissipation, but at a cost of 64 % reduction in puncture healing efficiency. This tradeoff is less pronounced when comparing permanent and dynamic networks. For films with similar thickness, DAP 0.7 networks exhibit a modest 10 % decrease in E_p^* while achieving a 3.5X higher healing efficiency by contrast to DDM 0.7 permanent networks, suggesting that temperature- and stress-induced dissociation of DA bonds enables effective puncture healing with minimal compromise in energy dissipation. More delocalization of the impact energy outwards from the impact point activating a variety of energy dissipation mechanisms is desired for high E_p^* while maintaining sufficient network bonds for recovery from the large biaxial extension of the membrane and avoidance of equatorial film fracture is essential for high η.

Moreover, the density of dynamic bonds had a significant influence on the material's performance under supersonic impact. Specifically, when a DAP 0.7 film ($h_0 = 224$ nm) was pre-heated at T ~ 80 °C before testing (Fig. S14), the dissociative nature of the dynamic network resulted in a 30 % reduction in bond density as compared to RT (22 °C) (Fig. S6). Consequently, the pre-heated film showed essentially no puncture healing ($\eta = -0.09$) and exhibited an E_p^* of 0.51 MJ kg^{-1} (~47 % lower than at RT) when impacted at $v_i \sim 450$ m/s. Films made with a lower density of dynamic crosslinks (DAP 0.4, $h_0 = 400$ nm) tested at RT not only had E_p^* values ~ 50 % less than DAP 0.7 ($h_0 = 435$ nm) but also lacked puncture-healing at $v_i > 300$ m/s. In the films with the highest density of dynamic bonds (DAP 1.0, $h_0 = 250$ nm), both the E_p^* and η values were similar to those in DAP 0.7 ($h_0 = 190$ nm). The final energy absorption and puncture healing performance of the films is determined by the interplay of film thickness and number density of dynamic bonds. For a given h_0, sufficient DA bond crosslink density is essential for higher E_p^* and η. By contrast, a thicker film increases η but reduces E_p^*. These effects are closely related to the thermomechanical history of the dynamic bonds established in DAP materials as discussed next.

Diels-Alder-polymer-enabled puncture-healing mechanism

By employing a thicker film and lower strain rates, the various deformation processes can be better separated from one another. For a 190-nm thick film impacted at ~ 300 m/s, the curved film cap adheres to the projectile as evidenced by imaging the cap-

Please cite this article in press as: Z. Sang et al., Materials Today (2025), https://doi.org/10.1016/j.mattod.2024.12.006

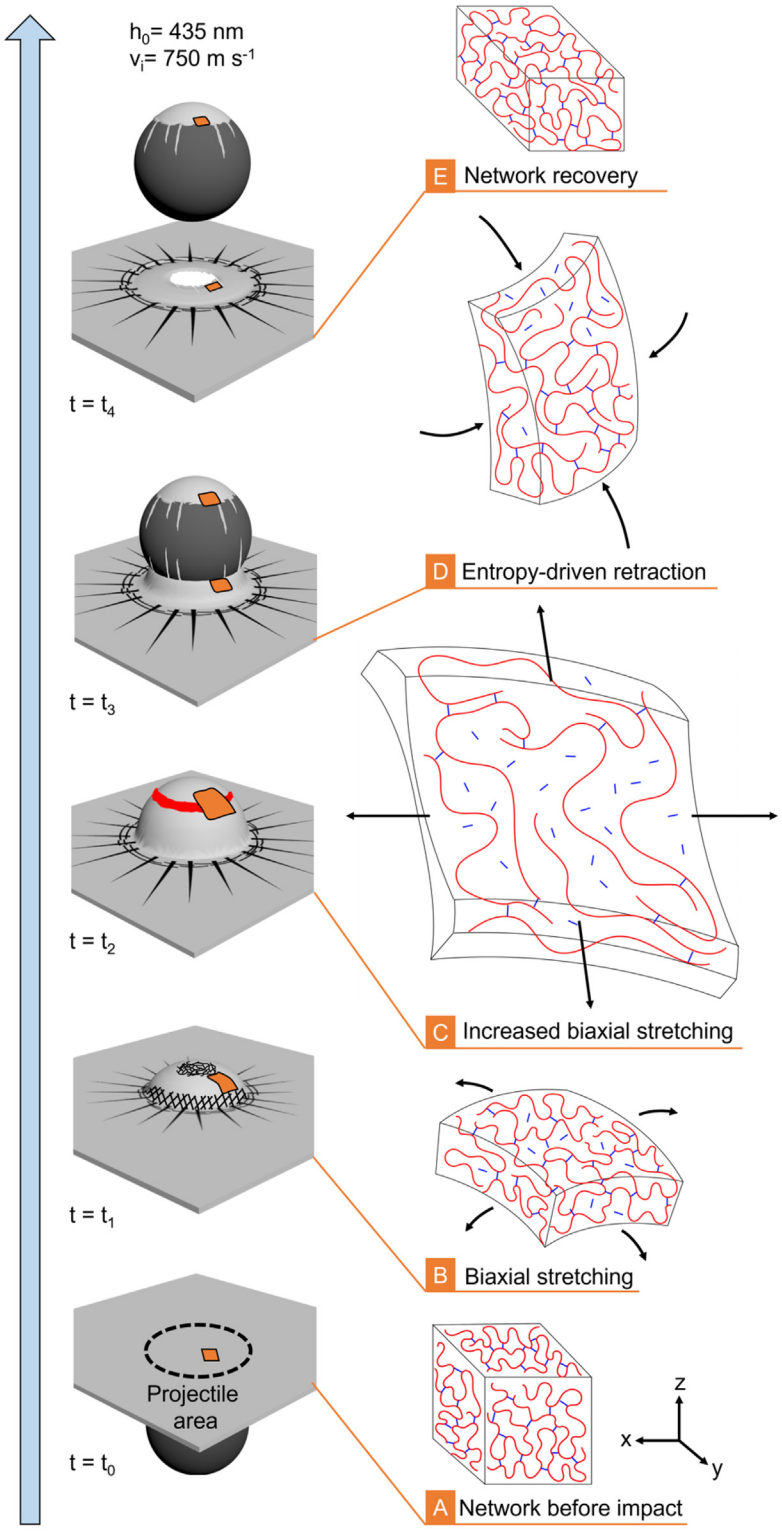

FIG. 4

μm and molecular scale 3D schematics of the deformation, puncture and healing processes in the Diels-Alder polymer network. The sequence of deformation and recovery during the perforation event is illustrated for the small orange region located within the (dashed line) impact region. Prior to impact ($t = t_0$, schematic A) the crosslinked network is below T_g and unoriented. During impact in schematic B, at a time t_1, radial and circumferential crazes and shear bands have formed at the cooler backside where $T < T_g$. By time t_2, these localized deformation features are erased due to additional adiabatic heating ($T > T_g$) and extensive biaxial network deformation as the T approaches T_{rDA}. After increased biaxial stretching as shown in schematic C, the thinner, higher temperature film fractures at time t_2 (circumferential red line) due to a lack of sufficient load-bearing DAP network chains. At t_3, in schematic D below the film fracture, the oriented, only partially dissociated and cooling network ($T_g < T < T_{rDA}$), undergoes entropy-driven elastic recovery with substantial perforation closure, and by time t_4 in schematic E, cooling has substantially re-established the DA network before the sample temperature drops below T_g. Outside the impact region, the temperature remains below T_g and the network polymer is only locally deformed at the positions of circumferential and radial crazes.

Please cite this article in press as: Z. Sang et al., Materials Today (2025), https://doi.org/10.1016/j.mattod.2024.12.006

tured projectile (Fig. 3c). The film backside near the center of the cap showed crazes and shear bands surrounded by an outer smooth, thinned region (40 % thinner at the outer edge). The deformation in the cap region occurred as a result of the widening and merging of radial and circumferential crazes at the film backside caused by equal biaxial stresses at the early impact time while T remained below the T_g. At higher impact velocities, the additional adiabatic heating of the film backside raised $T_g < T < T_{rDA}$, softening and allowing further thinning of the film which tends to erase the previously existing shear bands and crazes. Additionally, several molten, flattened, longitudinally oriented fibrils adhered to the side of the projectile because of the drawing of the partially dissociated DAP. Fig. 3d1 shows the backside of a 435-nm film impacted at 406 m/s, demonstrating a smooth conformal hemispherical cap surface, and Fig. 3d2 shows a FIB diametrical cross-section of this hemispherical cap. Following the black dashed line, the h_r/h_0 first gradually decreased from position 1 to 2 and eventually returned to 1.0 at position 5. The thinnest film region was located at position 2, adjacent to the north pole (initial impact location of the projectile). This region had a h_r/h_0 of 0.3, representing a biaxial stretching of ~ 170 %. Thin elongated "bridges" connect the film and the projectile (Fig. 3d3), indicative of stretching and orientation of adiabatic-shock- and viscoplastic-work-induced thermally softened DAP with reformation of dynamic bonds during cooling.

Based on post-impact morphological and chemical analysis, we propose the following sequence of deformation mechanisms leading to partial puncture-healing and energy dissipation of DAP films. The two main contributing effects to the dependence of the specimen temperature (T) vs time in the specimen are adiabatic shock heating and viscoplastic work. The state of stress (σ) in the specimen depends on the forces exerted by the projectile over time and the accommodating displacements of the sample over time. The T and σ depend on the particular location (radius r with respect to the impact center) and relative depth (z/h_o) in the sample, T $(r, \frac{z}{h_0}, t)$ and $\sigma(r, \frac{z}{h_0}, t)$. We have previously used equation of state (EOS) computations for a PS thin film under LIPIT impact to estimate the early time dependence of T and σ in a thin PS film [20]. Currently, there is no EOS available for DAP materials, but the PS computations are useful as a guide for the early stage behavior of the impact event. The initial part of the sample behavior is due to the adiabatic shock compression heating. At the shock front, the specimen temperature and pressure increase almost instantaneously. Then, as the compressive shock wave spreads out radially and passes a given specimen location, there is a brief interval of sample adiabatic cooling and stress relaxation. Then there is a 2nd increase in temperature and stress due to the projectile movement causing large amounts of viscoplastic work to the film at extreme strain rates that further raises the T and σ. Longer time behavior will be very challenging to model and would require information on material strain hardening vs thermal softening, including details of DA bond dissociation due to the combination of high T and high σ as well as the appearance of liquification (and possible sample ejecta) – which would then be followed after the perforation is complete (the perforation time is $\sim h_o/v_i \sim$ 10,000 ps (depending on film thickness h_o and impact velocity v_i) by viscoelastic recovery, puncture closure, and DA bond reassociation as the sample cools. The extent of DA bonding will depend on the time interval over the temperature range where DA bonds are remade. Specimen cooling is likely predominantly conductive (with some convective cooling since LIPIT is done in air) and perhaps takes milliseconds to seconds to drop the temperature down to ambient while freezing-in any unreacted DA bonds, chain orientation and residual stress once the temperature is below the glass transition. The appearance of distinctive deformation morphologies and recovery behaviors in the various regions of the impact due to their differing temperature and stress histories is evident from the analysis of impacted DAP films and captured projectiles. An additional factor contributing to the resultant healing behavior is enhanced mobility near free surfaces of thin films which is well-known in thermoplastics [35]. For instance, 30–50-nm thick free-standing high molecular weight PS (> 900 kDa) films showed a large, ~70 K, suppression of T_g. [36] The extent of the increase of chain mobility near the surfaces in our DAP thin films is, however, unknown, requiring future work to validate.

Notional 3D schematics at both the micron and molecular scale for the deformation and subsequent puncture healing processes within a DAP film (~ 435 nm) during projectile perforation at $v_i \sim$ 750 m/s are depicted in Fig. 4. By time t_1, within the orange-colored volume element shown in the impact circle of the projectile, the initial shock impact causes a rapid temperature rise on the film front side, accompanied by the formation of crazes and shear bands at the cooler backside surface. At time t_2, the biaxial stretching elevates the temperature for further film softening, reducing the DA bond density for the partially dissociated viscoelastic networks across the film volume in contact with the projectile. We speculate that likely a localized thin layer of liquified DAP with fully dissociated dynamic bonds occurs in the highest temperature projectile-film interface region resulting from the additional heating due to large interfacial shear stresses [20,37]. The resulting furan prepolymer and BMI liquid act like a lubricant, helping to minimize the amount of material dislodged by the projectile. The surrounding, weakly dissociated viscoelastic network ($T_g < T < T_{rDA}$) now undergoes additional stretching along the direction of projectile motion, thus further reducing the network entropy, thinning the film and absorbing energy. Then fracture occurs selectively at the boundary between the rigid upper region (indicated by the circumferential red line) and the near-liquid-like adjacent lower film portion, leaving the majority of the material in the impact region still attached to the film. The preserved material consists of partially dissociated networks that assist the puncture healing via entropy-driven elastic network recovery releasing strain energy [38]. Shape memory recovery facilitates hole closure (t_3 – t_4) and nearly full recovery of DA bonds.

The proposed mechanism and schematic for DAP-enabled supersonic puncture healing and energy dissipation are based on submicron-scale films impacted by micron-sized projectiles. When translating this behavior to the macroscopic scale, the E_p*- η relationship is currently unknown. Unpublished work from our group on an amorphous glassy thermoplastic suggests that the energy absorption is affected by the geometrical scaling size (for experiments varying h_0 from micron to mm, with a fixed

Please cite this article in press as: Z. Sang et al., Materials Today (2025), https://doi.org/10.1016/j.mattod.2024.12.006

$h_0/d_p \sim 0.24$), highlighting material responses evolve with changes in total impact event duration, strain and heating rates, stress state, and temperature gradients. Additional future scaling experiments are needed to provide deeper insights into the relationship between E_p*- η.

Conclusion

Diels-Alder covalent adaptive polymer networks can exhibit puncture healing along with energy absorption under supersonic impact. This behavior occurred in thin polymer films with dissociative dynamic bonds, exhibiting spatiotemporal gradients of thermomechanical responses to the extreme high-rate deformations that involve solid, viscoelastic, viscoplastic, and liquid states. The interplay of proposed mechanisms provides guidelines for further tuning the ballistic performance of dynamic network systems. The ability to form a low-viscosity interfacial lubricating fluid helps to minimize the amount of material carried away by the projectile, significant amounts of kinetic energy are dissipated via plastic deformation and bond dissociation and elastic network memory helps minimize the puncture. In addition to the thermomechanical mechanisms in the present DAP system, the performance can be enhanced by the introduction of additional dynamic bonds (such as hydrogen bonding) and / or dynamic covalent bonds of various types [14,16,19] that together can provide multiple mechanisms and stress levels and temperature–time intervals for bond re-shuffling during the impact event. Incorporating physical entanglements via a higher molecular weight prepolymer will strengthen the viscoplastic melt and aid in both energy dissipation and elastic recovery. The proposed design strategy opens the opportunity to innovate materials for widespread applications, well beyond ultrafast puncture-healable lightweight space debris protection.

Methods

Fabrication of ultra-thin films. The solvent-free synthesis of DAPs was described in our previous works[27,28]. Briefly, the linear prepolymer was synthesized via ring-opening polymerization of the epoxide monomer, NGDE, with FA added at a 1.9:1 epoxide-to-amine group ratio. The mixture was heated to 70 °C within 1 h, and the reaction was carried out under continuous stirring for 16 h, yielding a light-yellow viscous liquid. The weight average molecular weight of the resulting linear prepolymer was 7000 g mol^{-1}. The polydispersity index was 1.4, as determined by gel permeation chromatography. DAP was prepared by adding BMI crosslinkers at molar ratios of 0.4, 0.7, and 1.0 maleimide-to-furan groups at a temperature of 120 °C under mechanical stirring for 25 min. The calculated molecular weight between BMI crosslinks (M_c) is 889, 508, and 356 g mol^{-1}, respectively for the three molar ratios. Thin DAP films were prepared by completely dissolving DAP granules into the solution of toluene and DMF (v/v = 8:1) at 110 °C for 20 min, and the diluted solution (1–5 wt%, depending on the targeted h_0) was spin-coated onto a sacrificial-layer-coated (Polydiallyldimethylammonium chloride) silicon wafer [39] at 6000 rpm for 1 min, and the films were vacuum dried at 80 °C for 12 h). For the permanent crosslinked network DDM 0.7 sample, the NGDE was mixed with FA and DDM at 1.9:0.3 and 1.9:0.35 epoxide-to-amine ratio in a two-step manner, yielding the same crosslinked density as in DAP 0.7. The mixture was dissolved in toluene and spin coated. The DDM film was first heated at 70 °C for 16 h, followed by a post-curing of 6 h at 100 °C.

The various film thicknesses were tuned by varying polymer concentration and measured using a M−2000 automated-angle spectroscopic ellipsometer (J.A. Woollam Co., Inc.) (Fig. S1a). Film measurements were collected at four incidence angles: 45, 55, 65, and 75°. As shown in Fig. S1b, free-standing DAP films were obtained by separating the film from the silicon wafer onto the DI water with an angle of 60°, followed by adhering 200 mesh Ni TEM grids (Fig. S1c). After 12 h sitting atop the water, films were dried in air for 1 h, then annealed at 80 °C for 2 h. SEM images suggested a uniform, smooth, and defect-free film surface (Fig. S1d).

ATR-FTIR and variable-temperature FTIR. Bulk and ultra-thin films of DAP networks were measured in the attenuated total reflectance (ATR) mode using an ATR diamond crystal with a high-pressure clamp attachment and a mercury cadmium telluride (MCT) detector. Three-layer stacking of 357-nm-thick DAP 0.7 was used to ensure an enhanced signal of the ultra-thin film. The spectra were recorded between 4000 and 600 cm^{-1} at a resolution of 2 cm^{-1}. Variable-temperature FTIR (VT-FTIR) spectra were recorded using a custom-made sample stage (Harrick Scientific Products Inc) coupled to the FTIR (Bruker, Tensor II). About 100-μm-thickness DAP was cast onto a germanium waveguide. The spectra were detected from 4000 to 600 cm^{-1} at a resolution of 2 cm^{-1} in the attenuated total reflectance mode in the range of temperatures from 100 °C to 25 °C. The samples were cooled to each temperature and held for 10 min, and then three recordings were measured to ensure the stabilization of signals.

Infrared Nanospectroscopy (AFM-IR). AFM-IR imaging was done by a Nano-IR 3 (Bruker) coupled with a quantum cascade laser. Contact-mode AFM tips (GontGB-G AFM probe, NanoAndMore) were used to acquire IR spectra and a film height deflection map allowing imaging of deformation features. The deflection map was generated based on the position of reflected laser beam on AFM cantilever, detected by a photodiode [40]. The IR spectra were collected using a gold-coated AFM tip probe to detect the thermal expansion of the sample resulting from IR absorption. The detection volume was associated with film thickness and tip lateral spatial resolution (sub-20 nm). Three individual tips were used to ensure data reproducibility. The IR spectrum ranged from 1250 to 980 cm^{-1}, within one chip stage. Two spectra were collected from each point and averaged. A 435-nm-thick DAP 0.7 film was chosen to ensure sufficient signal-to-noise ratio and used to acquire local chemical information around the impact region, and ten individual perforations were measured. To avoid electron-beam-induced damage, AFM-IR samples were prepared separately and not imaged by SEM. Characteristic peaks (e.g., 1190 cm^{-1} of DA adduct and 1120 cm^{-1} of prepolymer) from AFM-IR were similar to the ATR-FTIR spectrum of bulk DAP.

Thermal characterization. TGA (TA instrument TGA 5500) was done for DAP 0.7, prepolymer, and BMI crosslinker in the temperature range between 100 and 500 °C under nitrogen atmosphere at a heating rate of 10 °C min^{-1}. T_g and T_{rDA} temperatures were determined via a DSC (TA instrument 2500)

Please cite this article in press as: Z. Sang et al., Materials Today (2025), https://doi.org/10.1016/j.mattod.2024.12.006

for DAP samples and permanently crosslinked DDM 0.7. Tzero aluminum pans filled with 8–10 mg of a sample were sealed hermetically, and the experiments were conducted at 5 °C min^{-1} ramping from −30 to 150 °C with a constant nitrogen gas flow of 50 mL min^{-1}.

Rheological analysis. The rheological measurements were performed using a TA Instruments DHR-2 Rheometer equipped with 40 mm diameter parallel plates. The gap distance was set to 1 mm. Viscosity measurements as a function of temperature ranging from 130 to 110 °C were carried out at a constant shear rate with the shear rates varing from 10^{-2} to 10^{3} s^{-1} (Fig. S7a). A steady-state shear flow test (Fig. S7b) was performed on the prepolymer at 60 °C by recording viscosity as a function of shear rate increasing from 10^{-1} to 10^{3} s^{-1}.

Wrinkling method. Elastomeric PDMS sheets (2 mm thick) were used to capture water-supported DAP films ($h_f/h_s \ll 1$), where h_f and h_s represent the thickness for deposited film and substrate, respectively. The bilayer specimens were air dried for 1 h, annealed at 60 °C for 4 h under vacuum, then transferred to a tensile stage (Kammrath Weiss). The uniaxial tensile strain was applied at a constant strain rate of 5 x 10^{-3} s^{-1}, and the lateral wrinkles were recorded by an optical microscope (DSX 500 Olympus) at 8 % strain. The wrinkle wavelength occurred parallel to the applied uniaxial tensile strain due to the transverse elastic compressive strain developed between the elastomeric PDMS substrate and the various DAP films. Averaging was done for 4–6 samples.

Micro-ballistic impact (LIPIT). Supersonic velocity impacts were carried out using LIPIT. In LIPIT, a single 3.7-μm-silica-projectile (microParticles GmbH, density 1900 kg m^{-3}) was accelerated from a launch pad and impacted the target under direct observation of high-speed imaging. The launch pad consisted of (bottom to top) a glass substrate (210 μm in thickness, Thermo Scientific), 50-nm-thickness gold coating, and 20-μm-thickness crosslinked PDMS (10:1 ratio, Sylgard 184, Dow Chemical). Microprojectiles were suspended in ethanol, drop-cast onto the launch pad, then spread out using a lab wipe (Kimberly-Clark Kim-wipe). One pulse of a Nd:YAG IR laser (10 ns pulse duration, 1064 nm) generated a local ablation of the gold, resulting in a rapidly expanding plasma on the launch pad, leading to rapid volume expansion of PDMS to accelerate the projectile. The velocity of the projectile was tuned by the excitation laser pulse energy using an attenuator. The projectile trajectory was illuminated by a second long duration laser pulse (Cavilux, Specialised Imaging, 640 nm wavelength, 30 μs duration) and imaged via an ultrahigh-speed camera with 3 ns exposure time (SIMX16, Specialised Imaging) consisting of 16 independently triggered intensified charge-coupled devices. The impact and residual velocities of projectiles were measured as indicated in Fig. S13 for incident projectile velocity.

Morphological characterization. All perforated samples were kept at −18 °C prior to imaging as a precaution to preserve the deformed film morphology. First, laser confocal scanning microscopy (LCSM, Keyence VX-K1100) was used to detect the shape and height profile of perforation morphology. Subsequently, a ThermoFisher Helios G4 FIB-SEM was employed to observe the uncoated polymer surface morphologies of the films at 1 keV, 21pA, 50 ns dwell time, using a through lens secondary electron detector (TLD). SEM imaging was done at an incidence angle of 85 degrees on a 45-degree pre-tilted sample holder. For FIB cross sectional milling, the samples were coated with 50 nm of gold and a high-energy Ga + ion beam (30 keV, 80pA) was employed to mill a cross-section of the impact region and in some instances, the arrested spherical projectile (see Fig. 3 and Fig. S11).

CRediT authorship contribution statement

Zhen Sang: Writing – original draft, Methodology, Investigation, Formal analysis, Conceptualization. **Hongkyu Eoh:** Methodology, Investigation. **Kailu Xiao:** Methodology, Investigation. **Dmitry Kurouski:** Methodology, Investigation. **Wenpeng Shan:** Methodology, Investigation. **Jinho Hyon:** Resources, Methodology. **Svetlana A. Sukhishvili:** Writing – review & editing, Supervision, Project administration, Investigation, Funding acquisition, Conceptualization. **Edwin L. Thomas:** Writing – review & editing, Supervision, Project administration, Conceptualization.

Data availability

Data will be made available on request.

Declaration of competing interest

The authors declare that they have no known competing financial interests or personal relationships that could have appeared to influence the work reported in this paper.

Acknowledgments

The authors acknowledge a Graduate Student Fellowship from the Hagler Institute for Advanced Study at Texas A&M University (Z. Sang). Uses of the TAMU Materials Characterization Facility (RRID: SCR_022202), the TAMU Soft Matter Facility, and Prof. George Pharr's SEM facility are also acknowledged.

Author contributions

Z.S., S.A.S., E.L.T designed the experiment and led this work. Z.S. fabricated samples, conducted micro-ballistic impact (LIPIT) experiments, drew schematics, and performed imaging techniques, along with other experiments and results interpretation. H. E. established LIPIT setup and provided technical support. D. K. helped with AFM-IR results interpretation. K.L.X, W.P.S, and J. H helped with discussion on sample preparation and data interpretations. S.A.S. and E.L.T supervised the project. Z.S, S.A.S, and E.L.T. wrote the manuscript with input from all authors.

Appendix A. Supplementary material

Supplementary data to this article can be found online at https://doi.org/10.1016/j.mattod.2024.12.006.

References

[1] E.L. Christiansen, J.H. Kerr, *Int. J. Impact Eng* 14 (1–4) (1993) 169.
[2] E. Grossman et al., MRS Bull. 35 (2010) 41.
[3] S.S. Sarva et al., *Polymer* 48 (8) (2007) 2208.
[4] S. Wang, M.W. Urban, *Nat. Rev. Mater.* 5 (8) (2020) 562.
[5] Y. Chen et al., *Nat Chem* 4 (6) (2012) 467.
[6] M.W. Urban et al., *Science* 362 (6411) (2018) 220.
[7] C. Li et al., *Angew. Chem.* 135 (46) (2023) e202313971.

Please cite this article in press as: Z. Sang et al., Materials Today (2025), https://doi.org/10.1016/j.mattod.2024.12.006

[8] Y. Yang, M.W. Urban, *Adv. Mater. Interfaces* 5 (17) (2018) 1800384.
[9] S.J. Kalista et al., *Polym. Chem.* 4 (18) (2013) 4910.
[10] S.J. Kalista Jr., T.C. Ward, *J R Soc Interface* 4 (13) (2007) 405.
[11] K.L. Gordon et al., NASA No. L-20545 (2017) .
[12] B.L. Lee et al., *J. Compos. Mater.* 35 (18) (2016) 1605.
[13] X. Chen et al., *Science* 295 (5560) (2002) 1698.
[14] C.J. Kloxin, C.N. Bowman, *Chem. Soc. Rev.* 42 (17) (2013) 7161.
[15] N.R. Boynton et al., *Science* 383 (6682) (2024) 545.
[16] P. Chakma, D. Konkolewicz, *Angew Chem Int Ed Engl* 58 (29) (2019) 9682.
[17] Y.S. Zholdassov et al., *Science* 380 (6649) (2023) 1053.
[18] G.M. Scheutz et al., *J. Am. Chem. Soc.* 141 (41) (2019) 16181.
[19] N. Zheng et al., *Chem Rev* 121 (3) (2021) 1716.
[20] J. Hyon et al., *ACS Nano* 15 (2) (2021) 2439.
[21] J. Hyon et al., *Mater. Today* 21 (8) (2018) 817.
[22] M. Capelot et al., *ACS Macro Lett* 1 (7) (2012) 789.
[23] M.C. Damien Montarnal, François Tournilhac, Ludwik Leibler, *Science* 334 (6058) (2011) 965.
[24] L. Yue et al., *ACS Macro Lett.* 9 (6) (2020) 836.
[25] C.M. Stafford et al., *Nat Mater* 3 (8) (2004) 545.
[26] J.Y. Chung et al., *Adv Mater* 23 (3) (2011) 349.
[27] Q. Zhou et al., *Adv. Funct. Mater.* 30 (30) (2020) 2002374.
[28] Z. Sang et al., *Chem. Eng. J.* 443 (2022) 136400.
[29] J.-H. Lee et al., *Science* 346 (6213) (2014) 1092.
[30] D. Veysset et al., *Appl. Phys. Rev.* 8 (1) (2021) 011319.
[31] E.P. Chan et al., *ACS Macro Lett* 8 (7) (2019) 806.
[32] D.L. Vezie et al., *Polymer* 36 (9) (1995) 1761.
[33] D. Kurouski et al., *Chem Soc Rev* 49 (11) (2020) 3315.
[34] W. Shan et al., *Macromolecules* 55 (21) (2022) 9594.
[35] M. Ediger, J. Forrest, *Macromolecules* 47 (2) (2014) 471.
[36] J.E. Pye, C.B. Roth, *J. Polym. Sci. B* 53 (1) (2015) 64.
[37] I. Mahmad Rasid et al., *Phys. Rev. Mater.* 4 (5) (2020) 055602.
[38] C.C. Hornat, M.W. Urban, *Nat. Commun.* 11 (1) (2020) 1028.
[39] S.H. Baxamusa et al., *Langmuir* 30 (18) (2014) 5126.
[40] Y.F. Dufrêne, *J. Bacteriol.* 184 (19) (2002) 5205.

Please cite this article in press as: Z. Sang et al., Materials Today (2025), https://doi.org/10.1016/j.mattod.2024.12.006